Microscale fabrication of 3D multicomponent metals via hydrogel infusion

Max Saccone (msaccone@caltech.edu)
Division of Chemistry and Chemical Engineering, California Institute of Technology
Rebecca A. Gallivan
Division of Engineering and Applied Science, California Institute of Technology
Kai Narita
Division of Engineering and Applied Science, California Institute of Technology
Daryl W. Yee
Division of Engineering and Applied Science, California Institute of Technology
Julia R. Greer
Division of Engineering and Applied Science, California Institute of Technology

Research Article

Keywords: metal, additive manufacturing, 3d printing, vat photopolymerization, digital light processing, hydrogels, organogels, in-situ material synthesis, copper, nickel, silver, tungsten, high entropy alloy

Posted Date: May 13th, 2022

DOI: https://doi.org/10.21203/rs.3.rs-1108933/v1

Version of Record: A version of this preprint was published at Nature on October 20th, 2022. See the published version at https://doi.org/10.1038/s41586-022-05433-2.

Abstract

Additive manufacturing (AM) of metals can enable rapid development of advanced parts with complex geometries, opening potential applications in the aerospace, automotive, and biomedical fields. Most existing metal AM techniques rely on costly thermally initiated melting or sintering processes, limiting the fabrication of materials with high thermal conductivity. Alternative vat photopolymerization methods require incorporating target materials or precursors into the photoresin, leading to increased viscosity, light scattering, and the need for a different resin composition for each material fabricated. To circumvent these problems with traditional metal AM techniques, we report an AM process where we infuse aqueous metal precursors into gels formed via vat photopolymerization and subsequently calcine and reduce the gels to form metal structures. Our streamlined technique enables the use of a single photoresin composition and varied post-processing conditions to fabricate a wide variety of metals and alloys with microscale resolution and highly twinned microstructures. We demonstrate fabrication of microlattices with <50 μm beam diameters formed from copper, nickel, silver, and alloys thereof, as well as high entropy and refractory alloys. We found that during the calcination process, the rate of mass loss associated with the exothermic combustion of the gel scaffold must be controlled to form dense parts. Microcrystalline microstructures with crystallographic annealing twin densities on the order of 10^6 m^{-1} were achieved. Our simple and compositionally flexible hydrogel-based approach to metal AM provides a pathway to fabricate new classes of metals with non-equilibrium microstructures and enhanced properties. Furthermore, our method is compatible with commercially successful vat photopolymerization techniques, showing a clear path to widespread adoption of this technique.

Summary Paragraph

Metal additive manufacturing (AM) enables the production of high value and high performance components[1,2] for aerospace[3,4], automotive[5,6], and biomedical applications[7,8]. Layer-by-layer fabrication circumvents the geometric limitations of traditional metalworking techniques, allowing topologically optimized parts to be made rapidly and efficiently[9–11]. Existing techniques rely on thermally initiated melting or sintering for part shaping, a costly and material-limited process[12–15]. We report an AM technique that produces metals and alloys with microscale resolution via vat photopolymerization (VP). 3D-sculpted hydrogels are infused with metal precursors, then calcined and reduced to convert the hydrogel scaffolds into miniaturized metal replicas. This approach represents a paradigm shift in VP; the material is selected only after the structure is fabricated. Unlike existing VP strategies, which incorporate target materials or precursors into the photoresin during printing[16–18], our method does not require re-optimization of resins and curing parameters for different materials, enabling quick iteration, compositional tuning, and the ability to fabricate multimaterials. We demonstrate AM of metals with critical dimensions of ~40 μm that are challenging to fabricate using conventional processes. Such

hydrogel-derived metals have unique and highly twinned microstructures; we demonstrate their link to measured mechanical properties, providing a pathway to create advanced metallic micromaterials.

Introduction

Metal AM is mostly achieved via costly powder bed fusion and directed energy deposition processes. Aluminum, magnesium, and titanium can be reliably produced[2,19–21] but often suffer from cracks and interfacial delamination due to repeated melting and solidification[12–15]. These processes also struggle to produce materials such as copper and silver ; high thermal conductivity and low laser absorptivity cause difficulties in thermal initiation and localization of melting or sintering[22,23].

A promising alternative class of techniques is VP, which uses light-initiated free radical polymerization to shape parts. Digital light processing (DLP) accomplishes this by projecting 2D images of UV light into a photoresin bath to cure an entire layer of the 3D structure simultaneously. DLP is capable of volumetric throughputs of up to 100 L/hr with a resolution of ~50 μm,[24] and has found varied commercial applications in the direct manufacturing of shoe soles[25], dental molds[26], and COVID-19 test swabs[27]. Although VP was developed predominantly for use with polymers[28], it has also been demonstrated for organogels[29], hydrogels[30], glasses[16] and ceramics[17,31]. However, material selection is still limited due to challenges with resin stability, processability, and synthetic accessibility associated with incorporating the necessary precursors into photoresins either as a slurry[32,33] or as an inorganic-organic mixture[34], and creating metals via VP has remained a challenge in the field. Oran *et al*. demonstrated AM of nanoscale silver by using hydrogels as “nanomanufacturing reactors”[35,36] in which two-photon activation guides the infiltration of precursors to volumetrically deposit 3D materials, and Vyatskikh *et al.* demonstrated AM of nanoscale nickel by using two-photon lithography to pattern inorganic-organic resins containing nickel acrylates, followed by pyrolysis and reduction by H_2[37]. However, these pioneering works are limited in scope for fabricating a wide variety of metals, requiring complex resin design and optimization, or tuning of conjugation chemistry for each new material. Other less common techniques such as direct ink writing (DIW) and material jetting (MJ) use, respectively, extrusion from a nozzle, and controlled deposition of a binder to define part shape. These methods circumvent the challenges of using heat to define part shape but struggle in other ways. Copper materials have been fabricated via DIW[38] and MJ[39], but neither of these techniques have been able to fabricate copper parts with feature sizes under 100 μm. These methods, like prior VP methods, require re-optimization based on the desired precursor; DIW requires tuning ink compositions to achieve a shear-thinning character, and MJ is sensitive to initial powder characteristics.

Results

Microscale metals fabricated via HI

We developed a VP-based AM technique, coined hydrogel infusion (HI), which enables fabrication of a wide range of previously inaccessible microscale metals and alloys from a single photoresin composition and simple post-processing treatments. We use 3D architected hydrogel scaffolds as platforms for subsequent *in-situ* material synthesis reactions, shown schematically in **Fig. 1a**. To fabricate metal microlattices, we use DLP (schematic in Supplementary Fig. 1) to print N,N-dimethylformamide (DMF)-/polyethylene glycol diacrylate (PEGda)-based architected organogels (see Supplementary Discussion 1 for resin design). DMF was chosen as a solvent for its low vapor pressure, which prevents compositional drift due to solvent evaporation during printing. The DLP printing step defines the shape of the final part; the designed octet lattice shape used throughout this work can be found in Supplementary Fig. 2, and details of the resin composition and DLP printing and swelling parameters can be found in Supplementary Table 1 and Supplementary Table 2. After printing, a solvent exchange replaces DMF with water, converting the organogels into hydrogels. The hydrogel structures are then soaked in a metal salt precursor solution to allow metal ions to swell the hydrogel scaffold. Calcination in air converts the metal salt-swollen hydrogels to metal oxides, and subsequent reduction in forming gas (95% N_2, 5% H_2) yields metal or alloy replicas of the designed architecture. Throughout the process, the part shape, defined during DLP printing, is maintained, with each dimension undergoing ~60-70% linear shrinkage, with a concomitant ~65-90% mass loss during calcination (see Supplementary Table 3 for shrinkage and mass loss several materials).

HIAM is a general process, theoretically compatible with any material with water-soluble precursors. We fabricated copper octet lattices; steps of the transformation from organogel to copper metal are shown in **Fig. 1b-e.** To fabricate copper, hydrogel structures were soaked in a 2M copper nitrate solution at 70˚C for 24 hours, followed by calcination at 700 ˚C (50 sccm air flow) and reduction at 900 ˚C (150 sccm forming gas flow).

To demonstrate the versatility of HIAM compared to previous gel-based VP AM techniques[31,35,40], we fabricated a variety of materials in addition to copper, including common metals Cu, Ni, Ag, and alloys thereof (see Supplementary Fig. 3), as well as more esoteric materials such as a CuNiCoFe high entropy alloy and the refractory alloy W-Ni (**Fig. 1f**). Additional development was required for these materials; fabrication and characterization of the CuNiCoFe high entropy alloy and the W-Ni alloy are described in Supplementary Figs. 4 and 5, and Supplementary Discussions 2 and 3, respectively. We also fabricated multimaterials such as the Cu/Co multimaterial shown in **Fig. 1g,h**. Compared to existing techniques which include precursors in the resin or introduce precursors through chemically directed swelling, HIAM enables facile traversing of a much larger compositional space, and significantly reduces the burden on resin design and/or developing conjugation chemistry, which may differ depending on the desired precursor.

HIAM is also distinguished by its ability to be parallelized; several organogels can be printed simultaneously, swelled in separate solutions, and then calcined/reduced together. **Fig. 1i** shows 8 hydrogel lattices (precursors of Cu, CuNi, CuNiCoFe, and CuNiCoFeCr) being simultaneously calcined to form oxides. This parallelization is impossible with any other form of metal AM and is a direct

consequence of the temporal separation of part shaping and material choice. Due to the versatility of HIAM for fabricating different materials, a large compositional space exists to be explored. From here on, we focus on one pure metal and one alloy: Cu and CuNi.

Structural characterization of micro-architected metals

The external and internal morphology of the metal microlattices were investigated by scanning electron microscopy (SEM) and a Ga^+-source focused ion beam (FIB) milling. SEM imaging reveals that Cu and CuNi samples maintained their octet lattice shape during thermal treatment (**Fig. 2a,e**), with beam diameters of ~ 40 μm (**Fig. 2b,f**). Using the FIB to mill out representative cross-sections in the lattice nodes, we observed that these materials were dense and relatively defect-free. The Cu showed a few < 5μm-diameter pores and a lamellar crack (**Fig. 2c**), while the CuNi alloy (**Fig. 2g**) was dense with similar μm-sized spherical pores as pure Cu, but no observed lamellar cracks. Energy dispersive X-ray spectroscopy (EDS) mapping showed homogenous distribution of Cu in the Cu lattice (**Fig. 2d**), and homogenous distribution of Cu and Ni in the CuNi lattice (**Fig. 2h**). See Supplementary Fig. 7 for structural characterization of additional materials including Ni, Ag, and CuAg alloy.

Chemical Characterization

We investigated the chemical composition of the metal microlattices using X-ray diffraction (XRD), energy dispersive X-ray spectroscopy (EDS), thermogravimetric analysis (TGA), and differential scanning calorimetry (DSC) to understand the chemical and microstructural evolution of these materials during calcination and reduction.

EDS analyses (see Supplementary Fig. 8) of Cu and CuNi microlattices show that these materials contain, by weight, 93% and 86% of the target materials, respectively. The balance is made up of carbon, which is difficult to accurately quantify and likely includes some adventitious carbon (see Supplementary Discussion 4), and aluminosilicate contamination from the furnace tubes.

EDS analysis shows that the atomic ratio of Cu:Ni in our CuNi material is 1.21:1, or a stoichiometric composition of $Cu_{55}Ni_{45}$. The deviation of alloy composition from swelling solution composition is likely due to different affinities of PEGda with the metal ions[41]. However, by adjusting the swelling solutions to account for preferential incorporation of certain ions, target compositions can be achieved with precision. For example, to target a $Cu_{50}Ni_{50}$ alloy, we swelled a hydrogel precursor in a 1:1.21 molar ratio of $Cu(NO_3)_2$:$Ni(NO_3)_2$. After calcination and reduction, EDS analysis showed that the stoichiometry of this cupronickel alloy was within 1% of the target composition, at $Cu_{50.5}Ni_{49.5}$ (see Supplementary Fig. 6).

Fig. 3 contains TGA and DSC data for Cu, and CuNi; equivalent data for additional materials studied is provided in Supplementary Fig. 9. Calcination of metal nitrate salt-containing gels in air (700 ˚C, 50 sccm) produces metal oxide replicas of the architectures. The XRD patterns (see Supplementary Fig. 10 for additional materials' XRD patterns) shown in **Fig. 3a** show that the calcined Cu precursor gel, which contained $Cu(NO_3)_2$, and the CuNi precursor gel, which contained $Cu(NO_3)_2$/$Ni(NO_3)_2$, were fully converted

to CuO and CuO/NiO respectively. Notably, the CuO/NiO XRD pattern shows the presence of the individual NiO and CuO phases in the calcined material. Reduction of these metal oxides in forming gas (900 ˚C, 150 sccm) converts the CuO and CuO/NiO lattices to Cu and a homogenous CuNi alloy, respectively (**Fig. 3b**). While both CuNi and Cu have face centered cubic crystal (FCC) structures, the single set of FCC reflections in the CuNi pattern shift to higher diffraction angles, a result of decreased lattice spacing due to the incorporation of the smaller Ni atom into the structure.

Fig. 3c contains TGA measurements of Cu and CuNi gels heated in air at 1 ˚C/min. The Cu and CuNi precursor gels, respectively, exhibit a similar mass loss profile to 12.7% and 15.8% of the original mass, reaching completion between 370 ˚C and 380 ˚C, indicated by mass stabilization at full conversion. The derivative of sample weight with respect to temperature, dW/dT, shows the regions of highest mass loss rate of ~1 wt.%/˚C that occur at 353 ˚C for Cu and at 331 ˚C for CuNi. Guides are placed at 110 ˚C, where initial dW/dT peaks occur for both Cu and CuNi, and 265 ˚C, where a subsequent dW/dT peak occurs for only Cu. **Fig. 3d** contains DSC profiles of Cu and CuNi precursor gels heated in air at 1 ˚C/min. Both gels exhibit similar normalized heat flow profiles; exothermic peaks begin at ~235 ˚C for both and reach a maximum heat flow of -1.5 W/g at 308 ˚C for Cu, and -2.6 W/g at 304 ˚C for CuNi.

Morphology and Microstructure Characterization

For the processing conditions reported here, HI-derived metals are microcrystalline, with randomly oriented micro-grains that are densely populated by annealing twins which generally form as the result of crystalline defects during grain growth or grain boundary motion[42]. The presence of micron-scale twinned regions in Cu is seen clearly in Ga^+ ion-channeling images (**Fig. 4a**, yellow arrows point to twins) and electron backscatter diffraction (EBSD) maps (**Fig. 4b)**.

Our materials have high crystallographic twin densities[43], defined as the length of twin boundary per cross-sectional area, of ~1.7×10^6 m^{-1} for Cu and 1.3×10^6 m^{-1} for CuNi. For Cu, each grain contains on average 4.8 twin boundaries, with 88% of all grains containing at least one twin boundary. CuNi has an average of 3.8 twin boundaries per grain, with 75% of grains containing at least one twin boundary. Additional twinning statistics as measured by EBSD are reported in Supplementary Table 4.

TEM analysis of HI-derived Cu (**Fig. 4c**) shows twins in more detail. We observe that grain boundaries and twin boundaries are well-formed, with no voids at triple junctions, and no observable secondary phases (i.e. unreduced CuO or amorphous carbon) besides the presence of aluminosilicate inclusions (see Supplementary Fig. 11 for TEM EDS) that result from contamination from the furnace tube (**Fig. 4d**). HI-derived Cu has an area-weighted average grain size of 13.74 8.43 μm, and CuNi has a grain size of 9.81 4.79 μm (**Fig. 4e**, insets). Grain size was measured via image analysis of SEM micrographs (see Supplementary Fig. 12) and corroborated by EBSD.

Mechanical characterization

Nanoindentation experiments performed on HI-derived Cu and CuNi revealed the hardness of Cu to be 1.81 0.37 GPa and that of CuNi to be 2.15 0.22 GPa. To contextualize these results, **Fig. 4e** contains a plot of nanoindentation hardness vs. grain size for the HIAM-produced Cu and CuNi in this work compared to data from literature for the same metals produced via traditional processing techniques (see Supplementary Table 5 for tabulated data). The plot also contains the expected hardness based on the Hall-Petch relation[44,45] $H = H_0 + kd^{-\frac{1}{2}}$, which relates nanoindentation hardness H to grain size d for ductile metals, where H_0 is an intrinsic hardness for a single crystalline material and k is a scaling factor related to grain boundary-induced hardening.

Twin boundaries are known to act as barriers to dislocation motion during deformation[43,46] and thus effectively increase measured hardness. To account for this effect, we introduce a modified Hall-Petch relation to account for the high twin boundary density[47]. The relative strength of the twin boundary in resisting deformation changes for various metals and alloys; to set an upper bound on twin-induced hardening, the twin boundaries are effectively treated as grain boundaries and the grain size d becomes $d_{eff} = D/(N+1)$, where N is the number of twin boundaries per grain (see Supplementary Discussion 7 for derivation of this expression). Since CuNi is far more sensitive to boundary impact on hardening than Cu (as evident by the 3.8 times larger k value in CuNi), there is a stronger effect of the twin boundaries even though there are ~25% less twins than Cu.

Discussion

Chemical composition and processing effects

TGA and DSC analyses of Cu and CuNi calcination reveal that the water initially bound to the hydrogel polymer network evaporates below ~100 ˚C, indicated by the endothermic heat flow of ~0.25 W/g present in the DSC profiles of both materials below 100 ˚C[53]. Multiple thermally induced processes occur simultaneously upon further heating. For example, between 100 ˚C and 400˚C, the Cu sample undergoes 1) dehydration of $Cu(NO_3)_2$ H_2O to anhydrous $Cu(NO_3)_2$, 2) thermal decomposition of anhydrous $Cu(NO_3)_2$, and 3) an exothermic combustion reaction[54] in which the nitrate salt acts as an oxidizer of the PEGda ($C_{26}H_{46}O_{13}$) polymer through the reaction

$$Cu(NO_3)_2 + \eta\, C_{26}H_{46}O_{13} + (31\eta - 2.5)O_2 \rightarrow CuO + 23\eta\, H_2O + 26\eta\, CO_2 + N_2,$$

where η the molar ratio of PEGda to nitrate salt, and 4) thermal decomposition of PEGda.

TGA and DSC profiles of the CuNi samples suggest a similar process, with a distinction being that the copper nitrate and nickel nitrate salts simultaneously decompose and act as oxidizers for polymer combustion.

Both Cu and CuNi precursor gels exhibit a strongly exothermic peak around 300 ˚C that is attributed to the combustion of the PEGda polymer scaffold. The rates and temperatures of maximum heat flow are -1.5 W/g at 308 ˚C for Cu, and -2.6 W/g at 304 ˚C for CuNi (**Fig. 3d)** and indicate that during calcination the CuNi gel releases heat more rapidly. This finding is consistent with our observation that the rate of maximum heat flow in the Ni gel is even higher, at -3.97 W/g at 333 ˚C (see Supplementary Fig. 9). The onset of this exothermic event is similar for Cu and CuNi, (~235 ˚C), while the onset of the corresponding event in pure Ni occurs at a significantly higher temperature of ~295 ˚C. This trend suggests that the heat released from the exothermic combustion of the copper nitrate salt in CuNi is sufficient to quickly increase the local temperature in the gel to the point where the nickel nitrate salt also contributes to the oxidation reaction at an apparently lower temperature, as is common in combustion synthesis[55].

The Cu and CuNi samples contain fewer defects and pores compared with pure Ni and Ag (see Supplementary Fig. 7). The presence of defects and pores is correlated with higher maximum dW/dT, quantified by TGA (see Supplementary Fig. 9). During calcination, samples undergo ~60-70% linear shrinkage and ~65-90% mass loss (see Supplementary Table 3), which drives kinetic competition between part shrinkage and internal pore formation. These findings indicate that rapid thermal decomposition inhibits global, isotropic part shrinkage and causes the formation of internal voids and pores; controlling and minimizing the rate of mass loss during thermal treatment steps is important for fabricating high quality parts via the HI method, consistent with other debinding processes. In practice, this necessitated slow ramping at 0.25 ˚C/min during calcination, and calcining at low pressure (~6 Torr).

Mechanical characterization and twinning

HI-derived metals contain a high density of annealing twins, formed without the ordinarily requisite melting and recrystallization[56], due to the complex interplay between kinetic processes (i.e., solid-state diffusion and grain nucleation) and thermodynamic grain coalescence during high-temperature calcination and reduction. Both Cu and CuNi exhibit higher hardness than the Hall-Petch predicted values even when corrected for twin boundary presence, by 47% and 15% respectively. While the spread in measured hardness can be attributed to variance in the locally probed microstructure (i.e. close proximity to twin boundaries and grain boundaries increasing hardness and the presence of micro-porosity reducing it), the greater average hardness is indicative of a global complexity in the material not explained by a simple microstructural mechanism, opening a new avenue for engineering and investigating complex material behavior.

Material selection after part shaping

In nearly every AM process to date, the material is decided prior part shaping, i.e., the AM material feedstock is often the desired material itself or is specifically formulated to contain precursors that can be subsequently converted into the desired material post-deposition. The composition of the fabricated structure is thus either that of the feedstock or of some clear derivative of it. To fabricate the same structure out of a different material necessarily requires the use of a different feedstock formulation. In

the context of ceramic and metal VP, this means that regardless of the slurry or inorganic-organic hybrid approach, the fabrication of each inorganic material requires an involved process of photoresin design and formulation, in addition to print parameter optimization.

HIAM is fundamentally different from the state of the art in that the material is selected after part shaping. A blank organogel structure fabricated from a single feedstock formulation can be transformed into a vast number of different compositions. Because the inorganic precursors are infused after part shaping, HIAM is unlike the traditional slurry or inorganic-organic hybrid resin approaches in that only a single photoresin composition needs to be designed and optimized for VP, which significantly simplifies the material development process. We've shown that this ability also allows HIAM to fabricate complex materials such as refractory metals and high entropy alloys, as well as multimaterial structures, a previously impossible task for VP. Finally, HIAM is not limited to VP and is generalizable to other polymer AM processes which can produce gels such as direct ink writing, or could be adapted to higher resolution VP via two photon lithography processes.

Conclusion

We developed an AM process to create microscale metal 3D structures using a facile and versatile VP approach. The conversion of metal salts within polymer scaffolds to metal oxides and their subsequent reduction to metals and alloys is a general process, requiring only that the target material has water-soluble precursors and that the intermediate oxide formed after calcination can be reduced by hydrogen gas. The ability to fabricate metallic materials using this accessible and high-resolution process provides new opportunities for fabrication of energy materials, micro-electromechanical systems, and biomedical devices. Hydrogel infusion represents a paradigm shift in AM, where the material is selected only after the part is shaped; directed infusion can create metallic multimaterials, and unprecedented compositional flexibility enables the fabrication of multicomponent alloys such as high entropy alloys and refractory alloys, known to have intermetallic phases which lead to superior high temperature behavior, and enhanced yield strength[57]. HIAM has direct implications for industrial use, as it provides a practical and powerful capability to integrate into the burgeoning and commercially advanced VP printing ecosystem.

Declarations

Acknowledgements

We thank Dr. Chi Ma for support and assistance with instruments in the Geological and Planetary Sciences Division Analytical Facility at Caltech, as well as Mingjie Xu for assistance with TEM experiments at UC Irvine Materials Research Institute. This work was supported by the U.S. Department of Energy, Office of Science, Basic Energy Sciences under Award #DE-SC0016945. M.A.S. acknowledges a graduate fellowship from the Resnick Sustainability Institute at Caltech. K.N. acknowledges a fellowship from the Masason Foundation.

Author contributions

M.A.S, D.W.Y, and J.R.G. conceived of and designed the experiments. M.A.S and D.W.Y designed the photoresin, printing parameters, and swelling protocol and fabricated samples. M.A.S, D.W.Y, and K.N. performed the thermal treatments and FIB/SEM/EDS experiments. M.A.S performed the DSC, TGA, and XRD experiments. R.A.G. performed the nanoindentation and EBSD experiments. All authors analyzed data and discussed the findings. M.A.S, D.W.Y, and J.R.G. wrote the manuscript. All authors edited and approved the manuscript.

Competing interests

K.N. founded the company 3D Architech, LLC, which has an exclusive option and right to acquire an exclusive license of intellectual property associated with this work (Patent US2020156035A1).

Additional information

Correspondence and requests for materials should be addressed to M.A.S, D.W.Y, or J.R.G.

References

1. Vafadar, A., Guzzomi, F., Rassau, A. & Hayward, K. Advances in Metal Additive Manufacturing: A Review of Common Processes, Industrial Applications, and Current Challenges. *Appl. Sci.* **11**, 1213 (2021).

2. Sames, W. J., List, F. A., Pannala, S., Dehoff, R. R. & Babu, S. S. The metallurgy and processing science of metal additive manufacturing. *Int. Mater. Rev.* **61**, 315–360 (2016).

3. Gisario, A., Kazarian, M., Martina, F. & Mehrpouya, M. Metal additive manufacturing in the commercial aviation industry: A review. *J. Manuf. Syst.* **53**, 124–149 (2019).

4. Mohd Yusuf, S., Cutler, S. & Gao, N. Review: The Impact of Metal Additive Manufacturing on the Aerospace Industry. *Metals (Basel).* **9**, 1286 (2019).

5. Leal, R. *et al.* Additive manufacturing tooling for the automotive industry. *Int. J. Adv. Manuf. Technol.* **92**, 1671–1676 (2017).

6. Mantovani, S. *et al.* Synergy between topology optimization and additive manufacturing in the automotive field. *Proc. Inst. Mech. Eng. Part B J. Eng. Manuf.* **235**, 555–567 (2021).

7. Wu, S.-H. *et al.* Porous Titanium-6 Aluminum-4 Vanadium Cage Has Better Osseointegration and Less Micromotion Than a Poly-Ether-Ether-Ketone Cage in Sheep Vertebral Fusion: Porous Ti Cage has Better Osseointegration than PEEK. *Artif. Organs* **37**, E191–E201 (2013).

8. Ahangar, P., Cooke, M. E., Weber, M. H. & Rosenzweig, D. H. Current Biomedical Applications of 3D Printing and Additive Manufacturing. *Appl. Sci.* **9**, 1713 (2019).

9. Attaran, M. The rise of 3-D printing: The advantages of additive manufacturing over traditional manufacturing. *Bus. Horiz.* **60**, 677–688 (2017).

10. Laureijs, R. E. *et al.* Metal Additive Manufacturing: Cost Competitive Beyond Low Volumes. *J. Manuf. Sci. Eng.* **139**, 81010 (2017).

11. Plocher, J. & Panesar, A. Review on design and structural optimisation in additive manufacturing: Towards next-generation lightweight structures. *Mater. Des.* **183**, 108164 (2019).

12. Svetlizky, D. *et al.* Directed energy deposition (DED) additive manufacturing: Physical characteristics, defects, challenges and applications. *Mater. Today* S1369702121001139 (2021). doi:10.1016/j.mattod.2021.03.020

13. Bartlett, J. L. & Li, X. An overview of residual stresses in metal powder bed fusion. *Addit. Manuf.* **27**, 131–149 (2019).

14. Sanchez, S. *et al.* Powder Bed Fusion of nickel-based superalloys: A review. *Int. J. Mach. Tools Manuf.* **165**, 103729 (2021).

15. Bajaj, P. *et al.* Steels in additive manufacturing: A review of their microstructure and properties. *Mater. Sci. Eng. A* **772**, 138633 (2020).

16. Zhang, D., Liu, X. & Qiu, J. 3D printing of glass by additive manufacturing techniques: a review. *Front. Optoelectron.* (2020). doi:10.1007/s12200-020-1009-z

17. Chen, Z. *et al.* 3D printing of ceramics: A review. *J. Eur. Ceram. Soc.* **39**, 661–687 (2019).

18. Yee, D. W. & Greer, J. R. Three-dimensional chemical reactors: *in situ* materials synthesis to advance vat photopolymerization. *Polym. Int.* **70**, 964–976 (2021).

19. Aboulkhair, N. T. *et al.* 3D printing of Aluminium alloys: Additive Manufacturing of Aluminium alloys using selective laser melting. *Prog. Mater. Sci.* **106**, 100578 (2019).

20. Liu, Z., He, B., Lyu, T. & Zou, Y. A Review on Additive Manufacturing of Titanium Alloys for Aerospace Applications: Directed Energy Deposition and Beyond Ti-6Al-4V. *JOM* **73**, 1804–1818 (2021).

21. Martin, J. H. *et al.* 3D printing of high-strength aluminium alloys. *Nature* **549**, 365–369 (2017).

22. Jadhav, S. D. *et al.* Surface Modified Copper Alloy Powder for Reliable Laser-based Additive Manufacturing. *Addit. Manuf.* **35**, 101418 (2020).

23. Robinson, J., Stanford, M. & Arjunan, A. Stable formation of powder bed laser fused 99.9% silver. *Mater. Today Commun.* **24**, 101195 (2020).

24. Gibson, I., Rosen, D. & Stucker, B. *Additive Manufacturing Technologies*. *Additive Manufacturing Technologies* (Springer New York, 2015). doi:10.1007/978-1-4939-2113-3

25. Kajtaz, M., Subic, A., Brandt, M. & Leary, M. Three-Dimensional Printing of Sports Equipment. in *Materials in Sports Equipment* 161–198 (Elsevier, 2019).

26. Unkovskiy, A. *et al.* Stereolithography vs. Direct Light Processing for Rapid Manufacturing of Complete Denture Bases: An In Vitro Accuracy Analysis. *J. Clin. Med.* **10**, 1070 (2021).

27. Manoj, A., Bhuyan, M., Raj Banik, S. & Ravi Sankar, M. 3D printing of nasopharyngeal swabs for COVID-19 diagnose: Past and current trends. *Mater. Today Proc.* **44**, 1361–1368 (2021).

28. Ligon, S. C., Liska, R., Stampfl, J., Gurr, M. & Mülhaupt, R. Polymers for 3D Printing and Customized Additive Manufacturing. *Chem. Rev.* **117**, 10212–10290 (2017).

29. Herzberger, J., Meenakshisundaram, V., Williams, C. B. & Long, T. E. 3D Printing All-Aromatic Polyimides Using Stereolithographic 3D Printing of Polyamic Acid Salts. *ACS Macro Lett.* **7**, 493–497 (2018).

30. Zhang, B. *et al.* Highly stretchable hydrogels for UV curing based high-resolution multimaterial 3D printing. *J. Mater. Chem. B* **6**, 3246–3253 (2018).

31. Yee, D. W. *et al.* Hydrogel-Based Additive Manufacturing of Lithium Cobalt Oxide. *Adv. Mater. Technol.* **6**, 2000791 (2021).

32. Corbel, S., Dufaud, O. & Roques-Carmes, T. Materials for Stereolithography. in *Stereolithography* (ed. Bártolo, P. J.) 141–159 (Springer US, 2011).

33. Nguyen, H. X., Suen, H., Poudel, B., Kwon, P. & Chung, H. Development of an innovative, high speed, large-scaled, and affordable metal additive manufacturing process. *CIRP Ann.* **69**, 177–180 (2020).

34. Vyatskikh, A. *et al.* Additive manufacturing of 3D nano-architected metals. *Nat. Commun.* **9**, 593 (2018).

35. Oran, D. *et al.* 3D nanofabrication by volumetric deposition and controlled shrinkage of patterned scaffolds. *Science (80-.).* **362**, 1281–1285 (2018).

36. Long, T. E. & Williams, C. B. Printing nanomaterials in shrinking gels. *Science (80-.).* **362**, 1244–1245 (2018).

37. Vyatskikh, A. *et al.* Additive manufacturing of 3D nano-architected metals. *Nat. Commun.* **9**, 593 (2018).

38. Mooraj, S. *et al.* Three-dimensional hierarchical nanoporous copper via direct ink writing and dealloying. *Scr. Mater.* **177**, 146–150 (2020).

39. Miyanaji, H. *et al.* Binder jetting additive manufacturing of copper foam structures. *Addit. Manuf.* **32**, 100960 (2020).

40. Yee, D. W., Lifson, M. L., Edwards, B. W. & Greer, J. R. Additive Manufacturing of 3D-Architected Multifunctional Metal Oxides. *Adv. Mater.* **31**, 1–9 (2019).

41. Sari, N., Kahraman, E., Sari, B. & Özgün, A. Synthesis of some polymer-metal complexes and elucidation of their structures. *J. Macromol. Sci. Part A Pure Appl. Chem.* **43**, 1227–1235 (2006).

42. Beyerlein, I. J., Zhang, X. & Misra, A. Growth twins and deformation twins in metals. *Annu. Rev. Mater. Res.* **44**, (2014).

43. Roy, B. & Das, J. Strengthening face centered cubic crystals by annealing induced nano-twins. *Sci. Rep.* **7**, 1–8 (2017).

44. Hall, E. O. The deformation and ageing of mild steel: III Discussion of results. *Proc. Phys. Soc. Sect. B* **64**, 747–753 (1951).

45. Cordero, Z. C., Knight, B. E. & Schuh, C. A. Six decades of the Hall–Petch effect – a survey of grain-size strengthening studies on pure metals. *Int. Mater. Rev.* **61**, 495–512 (2016).

46. Lu, L., Shen, Y., Chen, X., Qian, L. & Lu, K. Ultrahigh Strength and High Electrical Conductivity in Copper. *Science (80-.).* **304**, 422–426 (2004).

47. Pande, C. S., Rath, B. B. & Imam, M. A. Effect of annealing twins on Hall–Petch relation in polycrystalline materials. *Mater. Sci. Eng. A* **367**, 171–175 (2004).

48. Wang, C., Hossain Bhuiyan, M. E., Moreno, S. & Minary-Jolandan, M. Direct-Write Printing Copper-Nickel (Cu/Ni) Alloy with Controlled Composition from a Single Electrolyte Using Co-Electrodeposition. *ACS Appl. Mater. Interfaces* **12**, 18683–18691 (2020).

49. Emeis, F., Peterlechner, M., Divinski, S. V. & Wilde, G. Grain boundary engineering parameters for ultrafine grained microstructures: Proof of principles by a systematic composition variation in the Cu-Ni system. *Acta Mater.* **150**, 262–272 (2018).

50. Chang, S. Y. & Chang, T. K. Grain size effect on nanomechanical properties and deformation behavior of copper under nanoindentation test. *J. Appl. Phys.* **101**, (2007).

51. Bansal, S., Toimil-Molares, E., Saxena, A. & Tummala, R. R. Nanoindentation of single crystal and polycrystalline copper nanowires. *Proc. - Electron. Components Technol. Conf.* **1**, 71–76 (2005).

52. Bahr, D. F. & Vasquez, G. Effect of solid solution impurities on dislocation nucleation during nanoindentation. *J. Mater. Res.* **20**, 1947–1951 (2005).

53. Gun'ko, V. M., Savina, I. N. & Mikhalovsky, S. V. Properties of water bound in hydrogels. *Gels* **3**, (2017).

54. Danks, A. E., Hall, S. R. & Schnepp, Z. The evolution of 'sol–gel' chemistry as a technique for materials synthesis. *Mater. Horizons* **3**, 91–112 (2016).

55. Moore, J. J. & Feng, H. J. Combustion synthesis of advanced materials: Part I. Reaction parameters. *Prog. Mater. Sci.* **39**, 243–273 (1995).

56. Bahl, S. *et al.* Non-equilibrium microstructure, crystallographic texture and morphological texture synergistically result in unusual mechanical properties of 3D printed 316L stainless steel. *Addit. Manuf.* **28**, 65–77 (2019).

57. Senkov, O. N., Miracle, D. B., Chaput, K. J. & Couzinie, J. P. Development and exploration of refractory high entropy alloys - A review. *J. Mater. Res.* **33**, 3092–3128 (2018).

58. Lisi, N. *et al.* Contamination-free graphene by chemical vapor deposition in quartz furnaces. *Sci. Rep.* **7**, 1–11 (2017).

Methods

Fabrication of metal microlattices

3D printing resin preparation. 28 mL N,N-dimethylformamide (DMF; Sigma Aldrich, >99.9%) was mixed with 35 mL poly(ethylene glycol diacrylate) M_n = 575 (PEGda; Sigma-Aldrich). Separately, 347 mg 2-dimethylamino-2-(4-methyl-benzyl)-1-(4-morpholin-4-yl-phenyl)-butan-1-one (Irgacure 379; iGM Resins), 229 mg bis[4-(dimethylamino)phenyl]methanone (Michler's ketone; Sigma-Aldrich) and 10.3 mg 1-(phenyldiazenyl)naphthalen-2-ol (Sudan I; Sigma-Aldrich) was stirred into 7mL of DMF. This solution was then added to the DMF/PEGda mixture and swirled until completely homogenous.

Digital light processing 3D printing. The resin was formed into 3D organogel structures using a commercial 405 nm wavelength DLP 3D printer (Autodesk Ember). Lattice structures were designed consisting of octet lattices with 200 μm beam diameter and 1.5 mm unit cell size (see Supplementary Fig. 2).

Post-processing washes. After printing, the organogel lattices are yellow in color due to the presence of the UV blocker Sudan I. To remove unreacted photoresin components, each 3D printed organogel structure was soaked in DMF for 1 hr on a hot plate at 70 ˚C. After the first DMF rinse, the DMF was decanted, and organogel was soaked again in fresh DMF for 1 hr at 70 ˚C. After this process, the lattice appeared clear. Subsequently, each organogel structure was soaked in deionized (DI) water for 1 hr at 70

˚C, followed by a 2nd soak in fresh DI water for 1 hr at 70 ˚C to convert the structures from organogel lattices to hydrogel lattices. The solvent exchange step is needed to remove residual DMF in the structure, which can lead to formation of porosity upon calcination and reduction (see Supplementary Fig. 16). The presence of DMF can also cause precipitation of the metal salt during the swelling process, leading to an inhomogeneous distribution of the metal precursors.

Swelling in metal salt solutions. 2M solutions of copper nitrate, nickel nitrate, iron nitrate, cobalt nitrate, silver nitrate, chromium nitrate, and ammonium metatungstate were prepared with DI water. Hydrogel structures were immersed in the appropriate metal nitrate solution for 24 hr at 70 ˚C.

Calcination and Reduction. Metal ion-swelled hydrogel structures were calcined in a vacuum tube furnace (MTI OTF-1500X). The samples were placed in and covered by alumina boats within an alumina tube (MTI, 80 cm length, 51 mm inner diameter) that itself sat inside of a larger fused quartz tube (MTI, 1 m length, 92 mm inner diameter). The furnace was set up in this fashion to prevent copper vapors resulting from the heating process from interacting with the quartz tube, which has been shown lead to devitrification of the amorphous quartz tube and potential deposition of SiO_2[58]. The addition of the inner alumina tube significantly reduced the amount of SiO_2 particles observed after thermal treatment. During calcination, a 0.25 ˚C/min ramp rate was used up to a maximum temperature of 700 ˚C, followed by a 3 hr isothermal hold and cooling at 2 ˚C/min, under a compressed air flow of 50 sccm at a pressure of ~7 Torr. The slow ramp rate of 0.25 ˚C/min during calcination was found to be critical for controlling the highly exothermic decomposition of the nitrate salts and minimizing porosity in the fabricated samples.

Samples that contained silver nitrate salts produced elemental silver or silver composite lattices after calcination. All lattices except pure Ag were then reduced in forming gas at a flow rate of 150 sccm by heating at 3 ˚C/min to 900 ˚C or 700 ˚C (for CuAg) followed by a 6-hour isothermal hold, resulting in copper, nickel, homogenous cupronickel alloy, and heterogeneous copper-silver alloy lattices.

The calcined structures were then reduced in forming gas flowing at 150 sccm at a pressure of ~22 Torr, following a heating profile containing a 3 ˚C/min ramp to 900 ˚C, a 6 hr isothermal hold, and cooling at 3 ˚C/min.

Characterization and measurement

Scanning electron microscopy and focused ion beam milling. Samples were imaged via scanning electron microscopy (SEM; FEI Versa 3D DualBeam) at an accelerating voltage of 10-20 kV. Elemental analysis was performed in the same instrument using energy-dispersive X-ray spectroscopy (EDS; Bruker Quantax 200, XFlash 6|60 detector), with an applied voltage of 20 kV. Gallium focused ion beam (FIB) milling was performed in the same instrument to mill lattice cross-sections using an accelerating voltage of 30 kV and a current of 50 nA. FIB cleaning of the cross-sections was performed using an accelerating voltage of 16 kV and a current of 25 nA.

Electron backscatter diffraction. With the z-direction and build direction aligned, metal lattice samples were loaded into an Oxford EBSD System in a Zeiss11550VP SEM and are imaged using a 120 μm aperture at 20 kV. Data analysis for the Kikuchi maps was done in AztechHKL software. All maps display the inverse pole figure in the z-direction.

Transmission electron microscopy. Lamellae with thicknesses of <100 nm were prepared for transmission electron microscopy (TEM) using a liftout procedure in an SEM (FEI Versa 3D DualBeam). The top surface of the liftout region was protected with a ~100 nm-thick layer of platinum (Pt) deposited via a gas injection system (GIS), followed by a ~400 nm-thick layer of Ga^+ FIB-deposited Pt in the same chamber. Next, a Ga^+ ion beam was used to carve out trenches into the substrate forming a U-cut to free the ~1 μm-wide metal lamella base from the rest of the substrate. A tungsten needle (EZlift program) was attached to the lamella with FIB-deposited Pt before being cut free of the sample and transferred to a copper halfmoon grid. The lamella was attached to the Cu grid with FIB-deposited Pt and the tungsten needle was cut away to free the sample. After detaching the tungsten needle, a series of FIB cuts with a decreasing Ga^+ voltage/current (30kV/100pA; 30kV/10pA; 16kV/23pA) are used to progressively thin the cross-section of the lamella structure to <100 nm. TEM imaging was performed in a Jeol JEM-2800 TEM with a 200kV beam.

X-ray diffraction. Powder X-ray Diffraction (XRD; PANalytical X'Pert Pro) data was collected using a Cu $K\alpha_1$ source at 45 kV and 40 mA. Samples were either ground into powders or flattened and attached to an amorphous zero-background sample holder using clay prior to XRD analysis.

Thermogravimetric analysis. Thermogravimetric analysis (TGA; TA Instruments TGA 550A) was performed by heating samples to 700 ˚C at a rate of 1 ˚C/min in an air flow of 25 ml/min while the mass of the sample was continuously measured.

Differential Scanning Calorimetry. Differential scanning calorimetry (DSC; TA Instruments DSC 25) was performed by heating samples to 700 ˚C at a rate of 1 ˚C/min in an air flow of 25 ml/min while heat flow to the sample was continuously measured.

Nanoindentation. Samples were prepared for nanoindentation by mounting them in acrylic (Beuhler SamplKwik) and curing for 12 hours in silicone molds. The samples were polished first with 300 grit until the metal structure was exposed. The samples then were polished with 600 grit, followed by 1200 grit and subsequently a 0.25 μm grit suspension (Beuhler MetaDi Polycrystalline Diamond Slurry). Indentation was performed on an Agilent G200 Nano Indenter with XP module using a Berkovich tip with an area function given by . Samples were indented at 10^{-3} strain rate to a maximum depth of 1 μm, followed by a 2 second hold and subsequent unloading. Grain sizes were determined via SEM image analysis that consisted of tracing grains on the surface of the sample and using ImageJ to analyze the resulting shapes. These values were corroborated by EBSD mapping analysis of grain size.

Data and code availability

The data and code generated and/or analyzed during the current study are available from the corresponding authors on reasonable request.

Figures

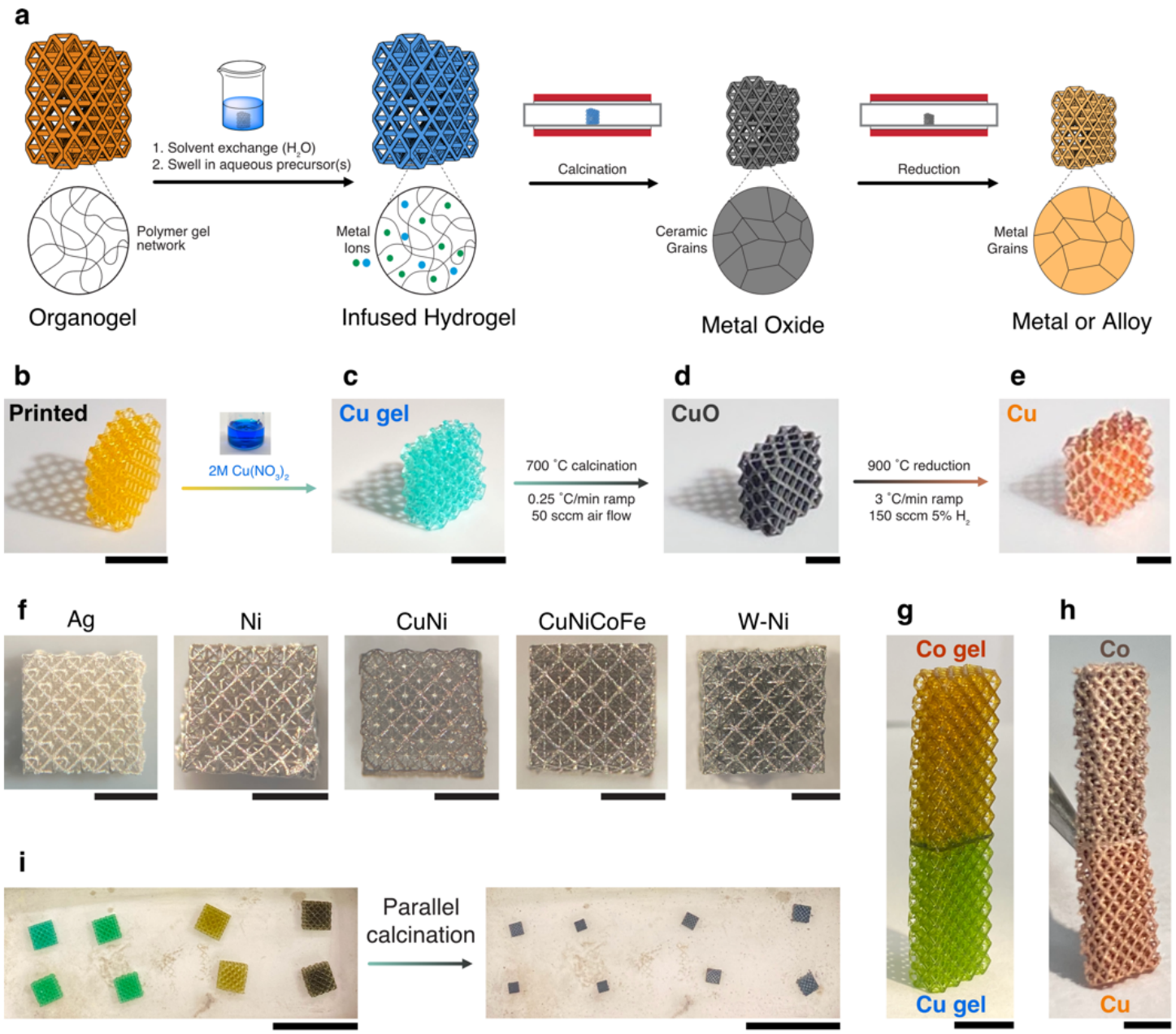

Figure 1

Hydrogel infusion AM process. a, Schematic of HIAM process. A PEGda-/DMF-based 3D printed organogel structure is converted to an infused hydrogel replica after leaching out photoactive compounds, solvent exchange, and infusing an appropriate aqueous precursor. Subsequent calcination in air forms metal oxide structures, which are reduced to pure metals in forming gas. **b-e,** HIAM process for Cu metal; 3D hydrogel was swelled for 24 hr at 70 ˚C in 2M $Cu(NO_3)_2$, calcined at 700 ˚C with 50 sccm air

flow, and reduced at 900 ˚C with 150 sccm forming gas flow. **f,** Additional metals fabricated via HIAM including metals Ag and Ni, binary alloy CuNi, high-entropy alloy CuNiCoFe, and refractory alloy W-Ni. **g,** An octet lattice infused with $Cu(NO_3)_2$ from one end, and $Co(NO_3)_2$ from the other. After calcination and reduction, the Cu/Co gel is transformed to **h,** a Cu/Co multimaterial. **i**, Parallel calcination of several different infused gels. Scale bars: **b,c,** 5mm; **d-f,** 1mm; **g,** 1 cm; **h,** 2mm; **i,** 2 cm.

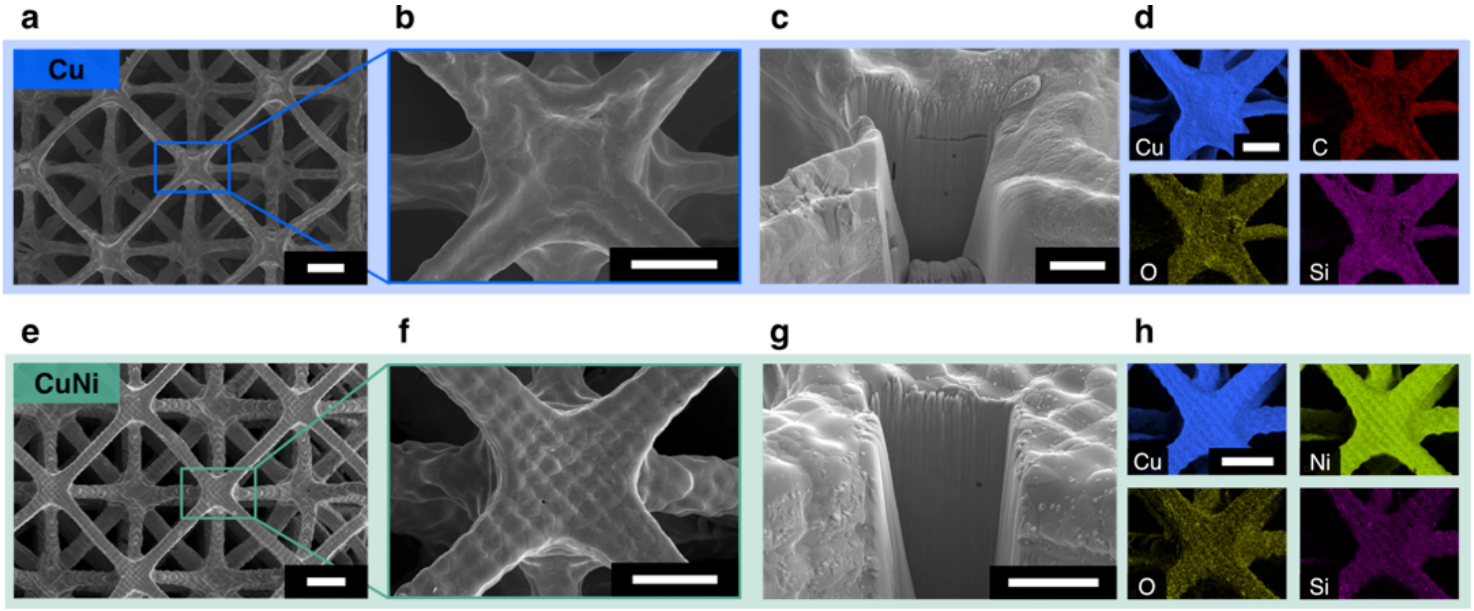

Figure 2

Morphology of Cu and CuNi microlattices. SEM images of Cu and CuNi octet lattices respectively showing **a,e,** multiple unit cells from the top, **b,f,** a single node, **c,g,** a FIB-milled cross-section showing the internal structure of a node from 52˚ tilt. **d,h,** EDS elemental mapping, showing uniform distribution of Cu in **d** and uniform distribution of Cu and Ni in **h**. Scale bars: **a,e,** 100 µm; **b,f,** 50 µm; **c,g,** 20 µm; **d,h,** 50 µm.

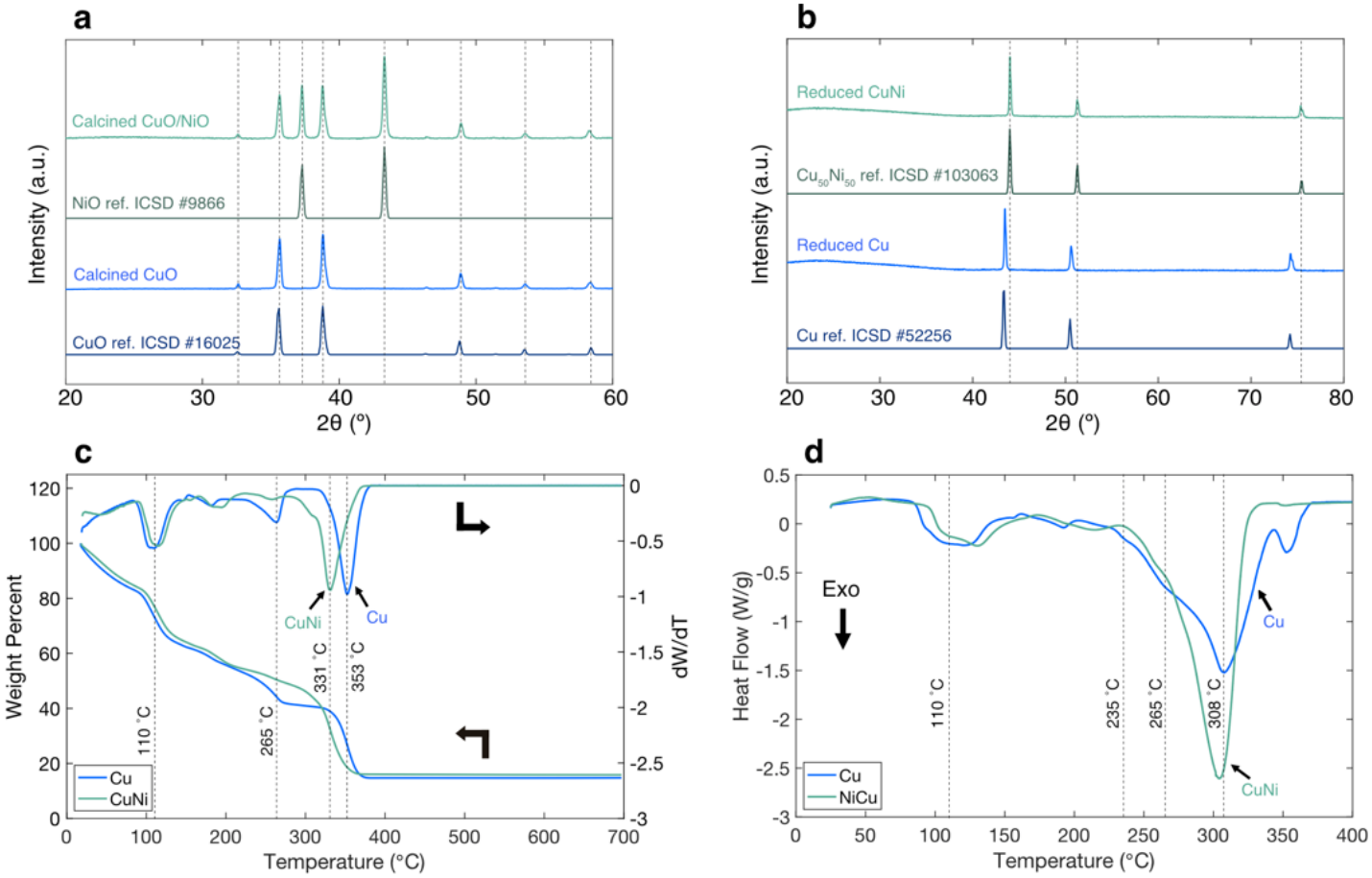

Figure 3

Chemical characterization of HI-produced metals and alloys. a, XRD patterns of calcined gels: $Cu(NO_3)_2$ gel is converted to CuO and $Cu(NO_3)_2/Ni(NO_3)_2$ gel is converted to CuO/NiO. **b**, XRD patterns of oxides reduced to parent metals: CuO is converted to Cu, and CuO/NiO is converted to a homogenous CuNi alloy, as evidenced by the single set of FCC reflections. **c**, TGA profiles of metal ion-infused gels heated to 700 ˚C in air at 1 ˚C/min reveal rapid mass loss events reaching maxima at 353 ˚C for Cu and 331 ˚C for CuNi. **d**, DSC profiles of metal ion-infused gels heated to 400 ˚C in air at 1 ˚C/min reveal exothermic events with maximum heat flow at 308 ˚C for Cu and at 304 ˚C for CuNi.

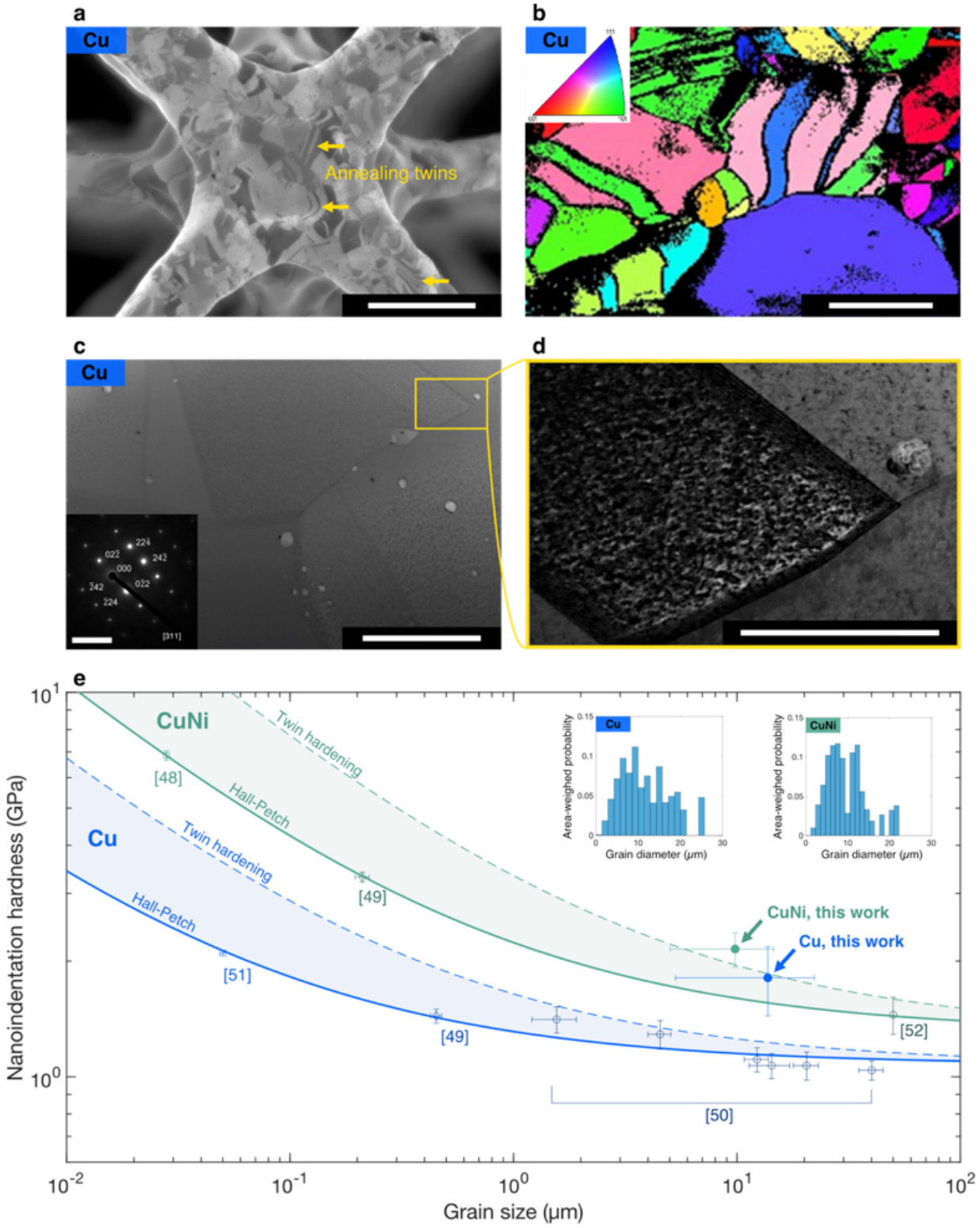

Figure 4

Microstructure and mechanical properties of HI-fabricated metals and alloys. a, Ga^+ ion-channeling image and **b**, EBSD maps of Cu show high densities of annealing twins. Cu has a complex micro-grained structure and multiple twinned regions within grains denoted by yellow arrows. **c,** TEM images of HI-derived Cu show well-formed grain boundaries, and some aluminosilicate inclusions. FCC copper is observed from the diffraction pattern in the inset of **c**. **d,** TEM image of a twin boundary and

aluminosilicate inclusion. **e,** Nanoindentation hardnesses of HI-derived Cu and CuNi samples are higher than reference nanoindentation data[48–52] and extrapolated Hall-Petch grain size scaling (dashed lines show correction for effect of twin-induced hardening). Error bars show standard deviations of grain size and nanoindentation hardness, where available. Insets: area-weighted grain size distribution for Cu and CuNi. Sample sizes: Cu hardness, n = 22; CuNi hardness, n = 44; Cu grain size, n = 246; CuNi grain size, n = 309. Scale bars: **a,** 50 μm **b,** 20 μm; **c,** 2 μm, inset 10 nm^{-1} **d,** 500 nm.

Supplementary Files

This is a list of supplementary files associated with this preprint. Click to download.

- SIHIAM1.docx